nature nanotechnology

LETTERS

PUBLISHED ONLINE: 27 JULY 2015 | DOI: 10.1038/NNANO.2015.156

Ballistic Josephson junctions in edge-contacted graphene

V. E. Calado[1†], S. Goswami[1†], G. Nanda[1], M. Diez[2], A. R. Akhmerov[1], K. Watanabe[3], T. Taniguchi[3], T. M. Klapwijk[1,4] and L. M. K. Vandersypen[1]*

Hybrid graphene–superconductor devices have attracted much attention since the early days of graphene research[1–18]. So far, these studies have been limited to the case of diffusive transport through graphene with poorly defined and modest-quality graphene/superconductor interfaces, usually combined with small critical magnetic fields of the superconducting electrodes. Here, we report graphene-based Josephson junctions with one-dimensional edge contacts[19] of molybdenum rhenium. The contacts exhibit a well-defined, transparent interface to the graphene, have a critical magnetic field of 8 T at 4 K, and the graphene has a high quality due to its encapsulation in hexagonal boron nitride[19,20]. This allows us to study and exploit graphene Josephson junctions in a new regime, characterized by ballistic transport. We find that the critical current oscillates with the carrier density due to phase-coherent interference of the electrons and holes that carry the supercurrent caused by the formation of a Fabry–Pérot cavity. Furthermore, relatively large supercurrents are observed over unprecedented long distances of up to 1.5 μm. Finally, in the quantum Hall regime we observe broken symmetry states while the contacts remain superconducting. These achievements open up new avenues to exploit the Dirac nature of graphene in interaction with the superconducting state.

The chiral nature of the charge carriers in graphene is predicted to give rise to specular Andreev reflection at the graphene/superconductor interface[21], and the quantum Hall effect can be strongly influenced by the interaction between edge states and a superconducting contact[22,23]. Such systems also provide a unique way to probe valley-polarized edge states[24], topological confinement in bilayer graphene[25], the interplay between superconductivity and quantum confinement, or ballistic two-dimensional Josephson junctions and their response to phase-coherent interference effects.

There are two important prerequisites that must be satisfied in order to observe any of these phenomena experimentally: (1) the graphene/superconductor interface should be transparent and well-defined and (2) the graphene must be of high electronic quality. In addition, for some of the above effects, a superconductor with a large upper critical field (H_{c2}) is required. Although significant technological progress has been made in improving the quality of graphene by either suspending it[26] or encapsulating it in hexagonal boron nitride (hBN)[19,20], the main challenge has been to combine such low-scattering graphene with a (large H_{c2}) superconductor. All reports on graphene–superconductor devices to date have involved superconducting contacts deposited directly on the graphene surface and diffusive transport through the device. In addition to the modest electronic quality of such devices, the use of top contacts leaves ambiguity as to where, exactly, the Andreev reflection takes place and under what spectral conditions; that is, it is not clear how far electrons travel beneath the contact before entering the superconductor.

To realize high-quality graphene–superconductor junctions we encapsulate graphene between two hBN crystals using the van der Waals pick-up method[19] (for details of device fabrication see Supplementary Information). This method ensures that the graphene is never in contact with any polymer during the stacking and thereafter. Electrical contact is made by metal deposition onto areas where the stack has been etched through. Unlike earlier work[19], where metal deposition was carried out in a separate lithography step, we begin by etching only the region to be contacted, followed immediately by metal deposition. This has the following advantages: (1) the contacts are self-aligned, thereby minimizing redundant metal overlap above the graphene and reducing the screening of electric and magnetic fields, and (2) combining the etching and deposition in one step minimizes resist residues at the contact interface, which is necessary to achieve transparent contacts. Instead of a normal metal, we sputter an alloy superconductor MoRe, which is attractive in several respects. First, MoRe is a type-II superconductor with a critical temperature of $T_c \approx 8$ K and an upper critical field $H_{c2} \approx 8$ T (at 4.2 K), which should easily allow for the observation of quantum Hall states, while the MoRe remains predominantly superconducting. Second, it has been shown that MoRe makes good electrical contact with carbon-based materials such as carbon nanotubes[27]. Considering the fact that edge-contact resistance can vary by an order of magnitude depending on the choice of metal[19], it is critical to select a superconductor that makes good electrical contact to the graphene. This is particularly important in the context of superconductor–graphene (S–G) Josephson junctions, where the transparency of the S/G interface directly affects the Andreev reflection. Furthermore, unlike surface contacts, such one-dimensional edge contacts ensure that the Andreev reflection occurs at a well-defined location, at the edge of the graphene, where it contacts the three-dimensional bulk superconductor. After deposition of the superconducting electrodes, the stack is etched into the desired geometry.

An optical image and a cross-sectional schematic of device A are shown in Fig. 1a–c. The graphene is etched into a rectangle with dimensions of $L = 1.5$ μm and $W = 2.0$ μm, with MoRe edge contacts on two sides. All measurements described here are performed in a (d.c.) four-point geometry, as shown in Fig. 1a. The MoRe leads are arranged such that the lead series resistance is minimized and the measured resistance is effectively the two-probe graphene resistance, irrespective of whether the MoRe is normal or superconducting.

[1]Kavli Institute of Nanoscience, Delft University of Technology, Delft, GA 2600, The Netherlands. [2]Instituut-Lorentz, Universiteit Leiden, PO Box 9506, Leiden, RA 2300, The Netherlands. [3]Advanced Materials Laboratory, National Institute for Materials Science, 1-1 Namiki, Tsukuba 305-0044, Japan. [4]Laboratory for Quantum Limited Devices, Physics Department, Moscow State Pedagogical University, 29 Malaya Pirogovskaya St., Moscow 119992, Russia. †These authors contributed equally to this work. *e-mail: l.m.k.vandersypen@tudelft.nl

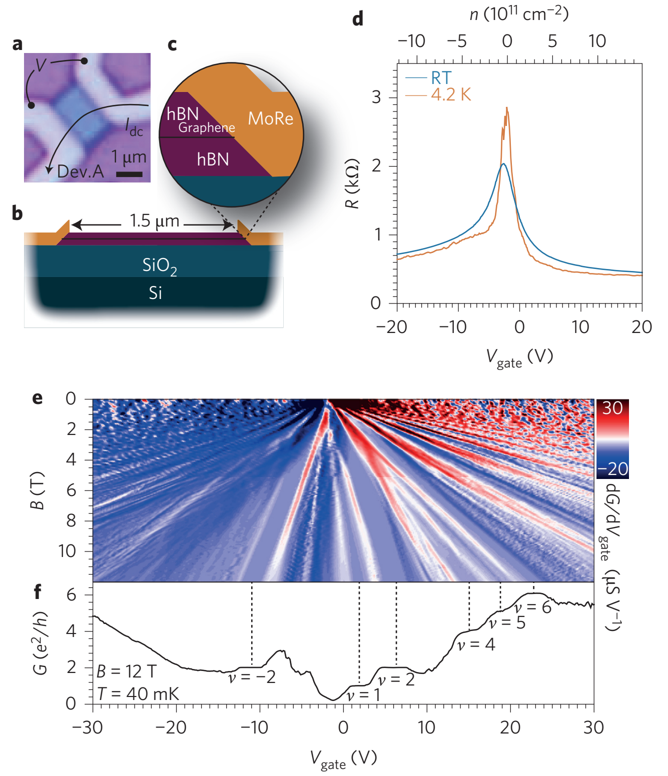

Figure 1 | High-quality hBN–graphene–hBN devices. **a**, Optical image of device A. A graphene/hBN sandwich (blue) is contacted on both sides from the edge with MoRe contacts (orange). The contacts are further split into two, which allows a (quasi-) four-probe measurement with minimal series lead resistance. **b**,**c**, Schematic cross-section of the device. **d**, Measured resistance R as a function of gate voltage V_{gate} at room temperature (RT) and at 4.2 K. The carrier density n is extracted from Shubnikov–de Haas oscillations. **e**, Numerically differentiated conductance with respect to gate voltage, dG/dV_{gate}, as a function of gate voltage and magnetic field, at 40 mK. **f**, Conductance G as a function of gate voltage at B = 12 T and T = 40 mK, showing symmetry broken states.

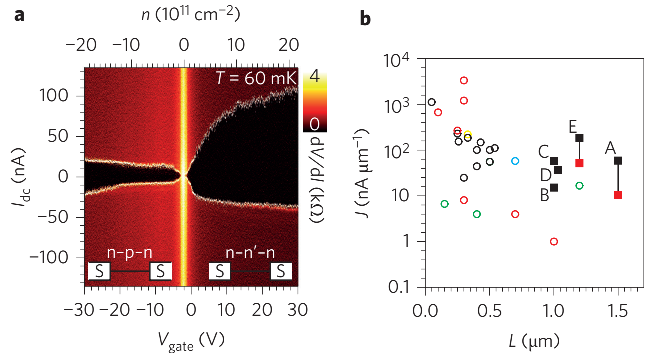

Figure 2 | Long-distance Josephson current in edge-contacted graphene. **a**, Differential resistance dV/dI as a function of applied d.c. current bias I_{dc} and gate voltage V_{gate}, at 60 mK. **b**, Critical current density J plotted as a function of device length L. Squares are the edge-contacted MoRe graphene devices A–E reported here. Black (red) squares correspond to a temperature of 50 mK (700 mK). More details about the temperature dependence can be found in Supplementary Fig. 1. Circles are data points taken from the literature[1–18]. Colours indicate the different superconductors used: black, Al; green, Nb/NbN/NbTiN; blue, ReW; red, Pb/PbIn; yellow, Pt/Ta.

This is important, because disordered superconductors such as MoRe have a large normal-state resistivity, potentially confusing the interpretation of the measurements when the electrodes turn normal (see Supplementary Fig. 4).

Figure 1d presents a plot of measured resistance R versus backgate voltage V_{gate} at room temperature and 4.2 K. A clear electron–hole asymmetry is visible, with the resistance in the hole-doped (p) regime being somewhat larger than that in the electron-doped (n) regime. We attribute this to contact-induced n-type doping, which leads to the formation of p–n junctions close to the contacts when the bulk of the graphene is p-doped. Such n-type doping effects from normal edge contacts have also been reported recently[28]. Figure 1e presents a Landau fan diagram recorded up to B = 12 T. The high electronic quality of the graphene is evident from the emergence of broken symmetry states above B = 5 T, which are well developed at B = 12 T (Fig. 1f). To our knowledge, this is the first observation of broken symmetry states in graphene with superconducting contacts. The plateaux on the electron side are better developed than those on the hole side, presumably a consequence of doping near the contacts.

At zero magnetic field, a gate-tunable supercurrent is observed through the device. Figure 2a plots the differential resistance dV/dI as a function of gate voltage V_{gate} and current bias I_{dc}. Evidently, the critical current I_c vanishes at the charge neutrality point, but reaches values in excess of 100 nA at V_{gate} = 30 V. The individual I_{dc}–V curves are hysteretic, as is evident from the asymmetry about I_{dc} = 0 (we discuss the possible origins of this hysteresis in Supplementary Fig. 1). On the hole side, I_c is considerably smaller, consistent with the formation of the conjectured n–p–n junctions. Figure 2b plots the critical current density per unit length, J, versus the Josephson junction length L, with data obtained from previous reports of graphene Josephson junctions shown as circles and data for the present MoRe edge-contacted devices as squares. The black squares show the critical current density at 50 mK, and the red squares show values at 700 mK. Note that the critical current density depends on the temperature and graphene carrier density, which vary from study to study. Despite this, it is clear that our MoRe edge-contacted devices stand out in terms of the relative magnitude of J compared to the earlier data. We find large supercurrent densities (up to ~200 nA µm^{-1}) over significantly longer distances (~1.5 µm). The observation of large supercurrents over an unprecedentedly long distance of 1.5 µm indicates the high quality of both the graphene itself and of the one-dimensional graphene/superconductor interfaces.

We also find unambiguous signatures of ballistic Josephson transport in this two-dimensional geometry. As shown in Fig. 3a, we observe for the first time clear oscillations in the critical current and the retrapping current when we vary the gate voltage, indicative of Fabry–Pérot interferences in the supercurrent through the junction. The transmission probability of the electrons and holes that carry the supercurrent is the result of the interference of trajectories that travel ballistically from one contact to the other with multiple reflections close to or at the edges of the graphene flake. As the gate voltage is varied, the Fermi wavelength changes, constructive and destructive interference alternate, leading to modulations in the critical current. One may expect the graphene/superconductor interfaces to form the walls of the cavity. However, we observe I_c oscillations only on the hole-doped side and not on the electron-doped side (Fig. 3d and the discussion below). This suggests that in the presence of n-doped regions near the MoRe/graphene interface, the relevant cavity is instead formed by p–n junctions near the contacts (inset, Fig. 3a). This gives rise to a reduced cavity length L_c. This length can be directly inferred from the period of the oscillations, extracted via a Fourier analysis (Supplementary Fig. 3) of these oscillations over many periods. A cavity length of L_c = 1.3 µm is found, which is smaller than the etched device length (L = 1.5 µm). A similar difference

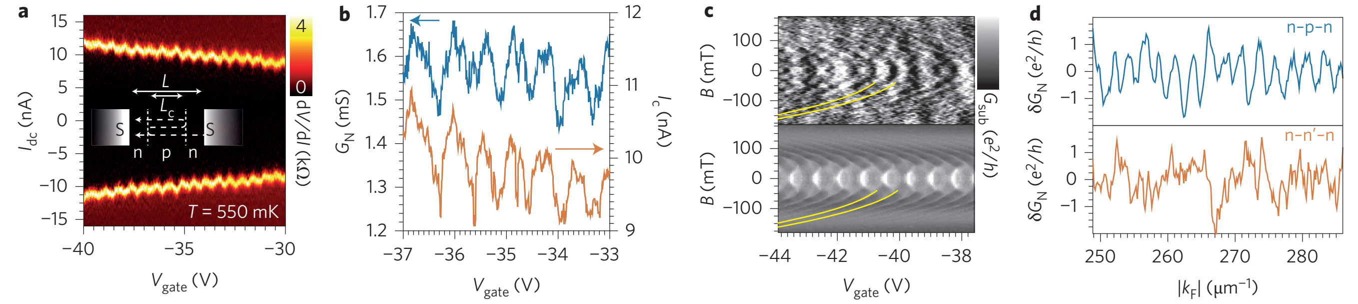

Figure 3 | Fabry–Pérot resonances in a Josephson junction. **a**, Differential resistance dV/dI as a function of applied d.c. current bias I_{dc} and gate voltage V_{gate}, at $T = 550$ mK. At 60 mK, statistical fluctuations in I_c make the effect much less visible. Inset: schematic of a cavity formed between p–n junctions due to doping near the contacts. Interference occurs due to reflections at the p–n junctions. **b**, Normal state conductance G_N and critical current I_c plotted as a function of gate voltage V_{gate}. **c**, Top: conductance measured as a function of magnetic field and gate voltage with $I_{dc} = 100$ nA. The dispersion of the Fabry–Pérot interferences follows a fourth-order polynomial (see equation (1)), plotted in yellow. See Supplementary Fig. 2 for a similar dispersion in device D. Bottom: simulated conductance for a cavity size of $L = 1.3$ μm and $W = 2$ μm. **d**, Top: conductance δG_N in the n–p–n regime as a function of absolute wavenumber $|k_F|$ in the central part of the device ($|k_F|$ is determined from the carrier density). δG_N is obtained after subtraction of a slowly varying background (see Supplementary Fig. 3 for details). Bottom: δG_N in the n–n′–n regime for the same wavenumber range. Here we attribute the fluctuations to UCF.

between device size and inferred cavity length was seen in device D (see Supplementary Fig. 3). This difference may arise from screening of the backgate near the contacts, in combination with the presence of the n-doped regions at the MoRe/graphene interfaces in both devices.

Interpretation of the oscillations in I_c in terms of Fabry–Pérot interference is further supported by comparing them with the oscillations in the normal state conductance G_N, measured at currents just above I_c. The oscillations of I_c with gate voltage clearly match the oscillations in G_N (Fig. 3b), as expected for Josephson junctions. In the case of normal state transport, we can apply a weak magnetic field perpendicular to the graphene to apply a Lorentz force to the trajectories of electrons and holes. This is expected to give a characteristic shift of the Fabry–Pérot resonances due to the accumulation of extra field-dependent phases. Indeed, in the measurements shown in Fig. 3c, we find that as B increases the main resonance features shift to a higher density, following a characteristic dispersion. To enhance the visibility we plot the quantity G_{sub}, which was obtained after subtracting a gate-dependent (but field-independent) modulation of the background conductance. The data are compared with the results of numerical simulations of the device conductance (see Methods for further details) in the ballistic regime with n–p–n junctions (Fig. 3c, lower panel). Simulation and experiment show an almost identical dispersion of the Fabry–Pérot resonances with magnetic field. It is also possible to obtain a semiclassical expression for the resonance condition (see Supplementary Information) by considering all the phases accumulated in the p-region of the n–p–n junction:

$$\frac{L_c}{\lambda_F(V_{gate})} = n_m + \frac{1}{2} + \frac{1}{6n_m}\left(\frac{L_c^2 eB}{h}\right)^2 \quad (1)$$

where n_m is a specific integer mode, $\lambda_F(V_{gate})$ is the Fermi wavelength, which is tuned by the backgate ($V_{gate} \sim 1/\lambda_F^2$), L_c is the cavity length, e is electron charge, and h is Planck's constant. The yellow curves in Fig. 3c are calculated using equation (1) for modes $n_m = -121, -120$ and show excellent agreement with the measured and simulated results. This provides strong evidence that the observed oscillations, both in I_c and G_N, arise from Fabry–Pérot interference, which implies phase-coherent ballistic transport. Although such oscillations due to Fabry–Pérot interference have been reported previously in a variety of systems including high-quality graphene with normal contacts[29,30], here we provide evidence for phase-coherent Fabry–Pérot interference in the supercurrent, which has not been observed before in any two-dimensional geometry.

To better understand the microscopic details of our device, the conductance in the n–p–n regime was compared with that in the n–n′–n regime (Fig. 3d). In the n–p–n regime (top panel) we observe periodic oscillations as a function of absolute wavenumber $|k_F|$, but universal conductance fluctuations (UCF) are seen in the n–n′–n case (bottom panel). We attribute these fluctuations to diffuse boundary scattering at or close to the graphene/MoRe interface. This diffuse scattering should also be present on the hole side, but does not dominate the transport due to the presence of the p–n junctions. Using the ballistic limit, with L much larger than the mean free path, where all resistance is from the contact interface, we can estimate a lower bound on the contact transparency T according to $G = (T/2)(4e^2/\pi h)k_F W$. From the conductance in the n–n′–n regime (Supplementary Fig. 3) we find a contact transparency of $T > 0.2$. In the n–p–n case, the conductance is dominated by the p–n barriers. In this case, the sharpness d of the p to n transition regions can be estimated according to $G_{npn} = (e^2/\pi h)\sqrt{(k_F/d)}W$. We find a sharpness of $d \approx 70$ nm, which is a plausible value considering the device dimensions.

As the d.c. Josephson effect is observed in these graphene devices over micrometre-scale distances, the magnetic field dependence of the critical current can also be explored for unusual geometries. Earlier reports have focused on graphene Josephson junctions with lengths much shorter than their width. In such a case, the magnetic field dependence of I_c is expected to follow the standard Fraunhofer diffraction pattern observed in tunnel junctions[31]. In the present devices, in contrast, the aspect ratio is close to 1, which has two consequences. First, unlike in tunnel junctions, the phase difference across the junction must be integrated along both interfaces. Furthermore, contributions involving reflections off the side of the junction must be included, especially when transport is ballistic[32–34]. The main prediction in this case is that the periodicity of I_c with magnetic flux becomes larger than a single flux quantum, $\Phi_0 = h/2e$. Despite significant differences across the patterns measured on the various devices, we consistently find a period larger than Φ_0, as seen in Fig. 4 for device A (and in Supplementary Fig. 5 for devices B and C). In contrast, earlier reports on graphene Josephson junctions all show flux periods smaller than Φ_0[1,2,5,7,9,12,13,16] before corrections to account for the London penetration depth.

The Fabry–Pérot oscillations in the critical current and the anomalous Fraunhofer diffraction patterns are mutually consistent

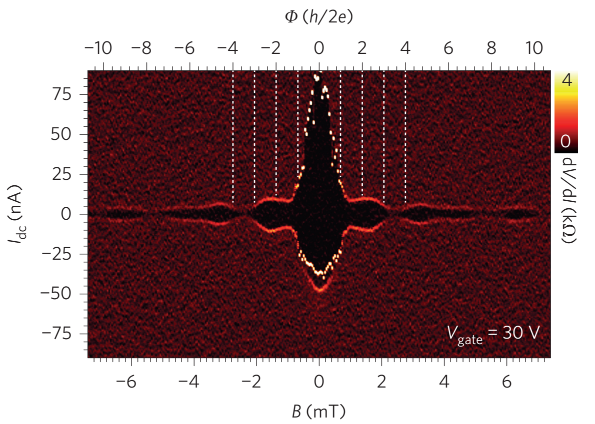

Figure 4 | Anomalous Fraunhofer diffraction pattern. Differential resistance dV/dI as a function of applied current bias I_{dc} and magnetic field B at a gate voltage of 30 V. We observe a separation between minima that clearly exceeds the flux quantum, $h/2e$.

and provide strong evidence of ballistic effects in superconducting transport through graphene. We believe that this is the first unambiguous demonstration of a ballistic Josephson junction in graphene.

Methods

Methods and any associated references are available in the online version of the paper.

Received 27 January 2015; accepted 17 June 2015;
published online 27 July 2015

References

1. Heersche, H. B., Jarillo-Herrero, P., Oostinga, J. B., Vandersypen, L. M. K. & Morpurgo, A. F. Bipolar supercurrent in graphene. *Nature* **446,** 56–59 (2007).
2. Du, X., Skachko, I. & Andrei, E. Y. Josephson current and multiple Andreev reflections in graphene SNS junctions. *Phys. Rev. B* **77,** 184507 (2008).
3. Miao, F., Bao, W., Zhang, H. & Lau, C. N. Premature switching in graphene Josephson transistors. *Solid State Commun.* **149,** 1046–1049 (2009).
4. Girit, C. *et al.* Tunable graphene DC superconducting quantum interference device. *Nano Lett.* **9,** 198–199 (2009).
5. Ojeda-Aristizabal, C., Ferrier, M., Guéron, S. & Bouchiat, H. Tuning the proximity effect in a superconductor–graphene–superconductor junction. *Phys. Rev. B* **79,** 165436 (2009).
6. Kanda, A. *et al.* Dependence of proximity-induced supercurrent on junction length in multilayer-graphene Josephson junctions. *Phys. C (Amsterdam, Neth.)* **470,** 1477–1480 (2010).
7. Choi, J.-H., Lee, H.-J. & Doh, Y.-J. Above-gap conductance anomaly studied in superconductor–graphene–superconductor Josephson junctions. *J. Korean Phys. Soc.* **57,** 149 (2010).
8. Borzenets, I. V., Coskun, U. C., Jones, S. J. & Finkelstein, G. Phase diffusion in graphene-based Josephson junctions. *Phys. Rev. Lett.* **107,** 137005 (2011).
9. Coskun, U. C. *et al.* Distribution of supercurrent switching in graphene under proximity effect. *Phys. Rev. Lett.* **108,** 097003 (2012).
10. Lee, G.-H., Jeong, D., Choi, J.-H., Doh, Y.-J. & Lee, H.-J. Electrically tunable macroscopic quantum tunneling in a graphene-based Josephson junction. *Phys. Rev. Lett.* **107,** 146605 (2011).
11. Rickhaus, P., Weiss, M., Marot, L. & Schönenberger, C. Quantum Hall effect in graphene with superconducting electrodes. *Nano Lett.* **12,** 1942–1945 (2012).
12. Popinciuc, M. *et al.* Zero-bias conductance peak and Josephson effect in graphene–NbTiN junctions. *Phys. Rev. B* **85,** 205404 (2012).
13. Komatsu, K., Li, C., Autier-Laurent, S., Bouchiat, H. & Gueron, S. Superconducting proximity effect through graphene from zero field to the quantum Hall regime. *Phys. Rev. B* **86,** 115412 (2012).
14. Mizuno, N., Nielsen, B. & Du, X. Ballistic-like supercurrent in suspended graphene Josephson weak links. *Nature Commun.* **4,** 2716 (2013).
15. Voutilainen, J. *et al.* Energy relaxation in graphene and its measurement with supercurrent. *Phys. Rev. B* **84,** 045419 (2011).
16. Jeong, D. *et al.* Observation of supercurrent in PbIn–graphene–PbIn Josephson junction. *Phys. Rev. B* **83,** 094503 (2011).
17. Borzenets, I. V. *et al.* Phonon bottleneck in graphene-based Josephson junctions at milli-Kelvin temperatures. *Phys. Rev. Lett.* **111,** 027001 (2013).
18. Choi, J.-H. *et al.* Complete gate control of supercurrent in graphene p–n junctions. *Nature Commun.* **4,** 2525 (2013).
19. Wang, L. *et al.* One-dimensional electrical contact to a two-dimensional material. *Science* **342,** 614 (2013).
20. Dean, C. R. *et al.* Boron nitride substrates for high-quality graphene electronics. *Nature Nanotech.* **5,** 722–726 (2010).
21. Beenakker, C. W. J. Specular Andreev reflection in graphene. *Phys. Rev. Lett.* **97,** 067007 (2006).
22. Hoppe, H., Zülicke, U. & Schön, G. Andreev reflection in strong magnetic fields. *Phys. Rev. Lett.* **84,** 1804–1807 (2000).
23. Chtchelkatchev, N. M. & Burmistrov, I. S. Conductance oscillations with magnetic field of a two-dimensional electron gas–superconductor junction. *Phys. Rev. B* **75,** 214510 (2007).
24. Akhmerov, A. R. & Beenakker, C. W. J. Detection of valley polarization in graphene by a superconducting contact. *Phys. Rev. Lett.* **98,** 157003 (2007).
25. Martin, I., Blanter, Y. M. & Morpurgo, A. F. Topological confinement in bilayer graphene. *Phys. Rev. Lett.* **100,** 036804 (2008).
26. Du, X., Skachko, I., Barker, A. & Andrei, E. Y. Approaching ballistic transport in suspended graphene. *Nature Nanotech.* **3,** 491–495 (2008).
27. Schneider, B. H., Etaki, S., van der Zant, H. S. J. & Steele, G. A. Coupling carbon nanotube mechanics to a superconducting circuit. *Sci. Rep.* **2,** 599 (2012).
28. Maher, P. *et al.* Tunable fractional quantum Hall phases in bilayer graphene. *Science* **345,** 61–64 (2014).
29. Young, A. F. & Kim, P. Quantum interference and Klein tunnelling in graphene heterojunctions. *Nature Phys.* **5,** 222–226 (2009).
30. Varlet, A. *et al.* Fabry–Pérot interference in gapped bilayer graphene with broken anti-Klein tunneling. *Phys. Rev. Lett.* **113,** 116601 (2014).
31. Tinkham, M. *Introduction to Superconductivity* 2nd edn (Dover, 2004).
32. Heida, J. P., van Wees, B. J., Klapwijk, T. M. & Borghs, G. Nonlocal supercurrent in mesoscopic Josephson junctions. *Phys. Rev. B* **57,** R5618–R5621 (1998).
33. Ledermann, U., Fauchère, A. L. & Blatter, G. Nonlocality in mesoscopic Josephson junctions with strip geometry. *Phys. Rev. B* **59,** R9027–R9030 (1999).
34. Sheehy, D. E. & Zagoskin, A. M. Theory of anomalous magnetic interference pattern in mesoscopic superconducting/normal/superconducting Josephson junctions. *Phys. Rev. B* **68,** 144514 (2003).

Acknowledgements

The authors thank V. Singh for sharing the MoRe sputtering recipe and C. Beenakker for discussions. The authors acknowledge support from the EC-FET Graphene Flagship, from the European Research Council (advanced grant no. 339306; METIQUM), from a European Research Council Synergy grant (QC-LAB) and from the Ministry of Education and Science of the Russian Federation (contract no. 14.B25.31.0007). This work is part of the Nanofront Consortium, funded by the Dutch Science Foundation OCW/NWO/FOM.

Author contributions

K.W. and T.T. grew the hBN crystals, G.N. fabricated the devices, V.E.C. and S.G. performed the measurements, and M.D. and A.R.A. carried out the numerical simulations and theory. The measurements were analysed and interpreted by V.E.C., S.G., M.D., A.R.A., T.M.K. and L.M.K.V. The manuscript was written by V.E.C., S.G. and L.M.K.V., with input from A.R.A., M.D. and T.M.K.

Additional information

Supplementary information is available in the online version of the paper. Reprints and permissions information is available online at www.nature.com/reprints. Correspondence and requests for materials should be addressed to L.M.K.V.

Competing financial interests

The authors declare no competing financial interests.

Methods

d.c. transport measurements. Low-temperature d.c. measurements were performed in a Leiden Cryogenics MCK-50 ^{3}He/^{4}He dilution fridge. The set-up was able to reach a base temperature of 40 mK and an electron temperature of ~70 mK. The d.c. currents and voltages were applied and probed with a home-built measurement set-up. The set-up was also equipped with a superconducting magnet coil capable of sustaining fields up to 12 T.

Tight-binding simulation. The Fabry–Pérot oscillations in the n–p–n junction were simulated by a tight-binding calculation using the Kwant software package[35]. The source code is part of the Supplementary Material. A 1.5 μm × 2.0 μm hexagonal lattice was discretized with a lattice constant of $a = 2$ nm, and with metallic leads on the 2.0-μm-wide sides. The contact-induced doping near both leads was modelled by a 100 nm region with a fixed chemical potential. The width of the transition region from the n to the central p region was set to 50 nm and modelled by $\tanh((x - x_0)/25\ \mathrm{nm})$. A finite contact resistance was imposed by reducing the transparency between the central strip and the leads to 60%. Finally, the transmission was calculated as a function of the Fermi wavenumber $k_F(\mu_p)$ and magnetic field B, resulting in the dispersion given in Fig. 3c.

References

35. Groth, C. W., Wimmer, M., Akhmerov, A. R., & Waintal, X. Kwant: a software package for quantum transport. *New J. Phys.* **16,** 063065 (2014).